



# Curved microchannels with inner wall expansion–contraction array for particle focusing

Ruihan Zhuang<sup>1,2</sup> · Kaixin Song<sup>1,2</sup> · Zhibin Wang<sup>1,2,3</sup> · Gang Chen<sup>4</sup> · Ying Chen<sup>1,2</sup> · Lisi Jia<sup>1,2</sup>

Received: 30 November 2023 / Accepted: 31 January 2024 / Published online: 15 March 2024  
© The Author(s), under exclusive licence to Springer-Verlag GmbH Germany, part of Springer Nature 2024

## Abstract

To enhance focusing performance, we proposed an integrated microchannel with expansion–contraction arrays (ECA) on the inner wall of the curved microchannel (CIECA) and compared it with a straight microchannel with ECA (SECA) as well as the traditional integrated microchannel of ECA on the outer wall of the curved channel (COECA). We investigated the particle-focusing mechanisms in these microchannels through a combination of experiments and numerical simulations. The proposed integrated microchannel demonstrates significant improvements in focusing performance compared to SECA and COECA, which is attributed to its consistent Dean flow. In contrast, COECA shows the poorest performance because of inconsistent Dean flow. The focusing width in the proposed integrated microchannel is reduced to 1/3 of that in COECA and 1/2 of that in SECA. Furthermore, the focusing performance of CIECA improves as the Reynolds number increases, eventually forming a single trajectory when the Reynolds number (at contraction) reaches 83.33. Finally, the impact of particle size on focusing performance was investigated through numerical simulations. The focusing performance of the CIECA is the best in these three microchannels. In CIECA, as the particle size increases, the focusing width initially decreases and then increases. Among them, 8 and 10  $\mu\text{m}$  particles can achieve complete focusing. This study serves as a crucial reference for comprehending and enhancing particle focusing through the synergy of multi-Dean flow.

**Keywords** Inertial focusing · Curved microchannel · Expansion–contraction array · Multi-Dean flow

## 1 Introduction

The manipulation of micrometer-sized particles carries substantial potential applications in the fields of chemistry, biology, and life sciences. Particularly, the analysis, counting, and filtration of particles play an increasingly crucial role in biochemical analysis, disease diagnosis, environmental

monitoring, and various other domains (Lim et al. 2012; Jin et al. 2014; Li et al. 2016; Roper 2016). Among these processes, particle focusing is a crucial preprocessing step, which involves arranging randomly dispersed particles into one or more streamlines to facilitate subsequent tasks. A comprehensive understanding of the focusing mechanism within channels is paramount, as it greatly facilitates subsequent tasks, enhancing the overall efficiency and accuracy of various biological assays, diagnostic processes, and analytical procedures. Recently, microfluidics (Qin et al. 2023; Wang et al. 2018) has garnered significant attention as a tool of particle focusing, leveraging its ability to manipulate microscale flows and microparticles precisely. The evolution of microfluidic techniques has resulted in the classification of particle focusing into two fundamental approaches: active and passive methods. In contrast to alternative active strategies utilizing external forces such as acoustic (Augustsson et al. 2012), thermal (Wang et al. 2019), electrical (Çetin and Li 2011), and magnetic forces (Forbes and Forry 2012), passive particle-focusing methods have gained considerable attention due to their inherent

✉ Zhibin Wang  
wangzhibin@gdut.edu.cn

<sup>1</sup> School of Materials and Energy, Guangdong University of Technology, Guangzhou 510006, China

<sup>2</sup> Guangdong Provincial Key Laboratory of Functional Soft Condensed Matter, Guangzhou 510006, China

<sup>3</sup> Key Laboratory of Low-Grade Energy Utilization Technologies and Systems (Chongqing University), Ministry of Education of China, Chongqing University, Chongqing 400044, China

<sup>4</sup> School of Energy and Power Engineering, Zhengzhou University of Light Industry, Zhengzhou, Henan 450002, China

advantages, including simplified processing, streamlined operation, and cost-effectiveness.

Inertial focusing, as one of the passive methods, has garnered considerable attention in recent decades owing to its simple structure, high throughput, and non-invasive nature (Xiang et al. 2019; Fan et al. 2019). The inertia focusing of particles was first discovered by Segrè and Silberberg (1961). Through experiments conducted in a circular tube, they observed that particles tended to aggregate at a distance of approximately 0.6 times the radius from the center of the tube. Subsequently, with the rapid development of microfluidic technology, Bhagat et al. (2008) conducted a study on the focusing behavior of particles in a straight channel with a rectangular cross section, revealing insights into the dynamics of particle focusing on such geometries. In addition, the particle size and flow velocity have a significant influence on the number of focusing positions for particles, posing challenges for subsequent tasks such as analysis and counting (Zhou and Papautsky 2013; Prohm and Stark 2014; Liu et al. 2015; Lu et al. 2017). In the straight channel, particles undergo lateral migration toward equilibrium positions driven by a combination of shear gradient lift force toward the wall and wall-induced lift toward the center of the channel (Zhang et al. 2016). Smaller particles experience a weaker inertial lift force, requiring a longer channel for effective focusing. However, meeting this requirement for elongation increases both the microfluidic chip's area and pressure. Consequently, the additional transverse force was strategically applied to the particles, resulting in a notable reduction in the number of equilibrium positions and an effective enhancement in the compactness of microfluidic chip focusing. Both the curved microchannel and the expansion–contraction arrays (ECA) have been extensively employed to induce the Dean flow, a distinctive secondary flow. Dean flow exerts drag force on particles in the direction of the channel cross section, accelerating particle migration in that direction and thereby enhancing particle focusing (Zhao et al. 2020). Bhagat et al. (2010) designed a sheathless planar spiral microfluidic chip, utilizing both Dean drag force and inertial lift force to achieve three-dimensional inertial focusing of 6  $\mu\text{m}$  particles. Guan et al. (2013) enhanced Dean flow further by incorporating a trapezoidal cross section in a spiral channel, accelerating particle migration in the cross-sectional direction and achieving rapid focusing of particles with various sizes. Despite a significant improvement in focusing compared to straight channels, achieving particle focusing with certain methods still requires a sufficiently long channel to ensure optimal performance. Lee et al. (2009) proposed an ECA microchannel for cell focusing. The study found that the ECA structure induces Dean flow, thereby enhancing the focusing efficiency of cells. Wang et al. (2023) introduced multiple sheath fluids into a rectangular ECA, enhancing

the Dean flow induced by this structure. This improvement resulted in a significant enhancement of particle focusing and sorting capabilities. While the mentioned ECA could only generate Dean flow locally, there is still room for further improvement in particle-focusing efficiency.

As a response to this, some researchers have proposed a sheathless spiral microchannel that combined the ECA on the outside of the curved microchannel or micro-obstacles in the spiral microchannel for particle focusing and separation (Shen et al. 2017; Tang et al. 2020; Gou et al. 2020). Despite these studies employing a combination of curved microchannels and ECA or micro-obstacles to achieve particle focus, there has been a lack of visualization of the coordinated focusing mechanism using a combination of ECA and a curved microchannel. Moreover, these studies have not thoroughly demonstrated the potential impact of such combinations on focusing performance. Confirming the effectiveness of the curved microchannel and ECA combination could lead to a substantial reduction in channel length. Nonetheless, Shen et al. (2019) utilized microbarriers in conjunction with spiral channels to achieve focused particles with a channel length of 25 cm. Similarly, Gou et al. (2020) integrated the ECA and the spiral microchannel to realize inertial focusing with a total length of 31.8 cm. We believe that the orientation of the ECA integrated into the curved microchannel determines the Dean flow direction, which subsequently influences particle migration. If the Dean flow induced by the ECA aligns consistently with that induced by the curved microchannel, the particle migration effects of these two structures can synergize, potentially leading to enhanced focusing performance. Additionally, the rational integration of the curved microchannel and ECA could reduce the length required for particle focusing. Therefore, in-depth research and comprehensive studies are essential to thoroughly understand the interaction between the Dean flows induced by the ECA and the curved microchannel.

Consequently, we have developed a sheathless curved microchannel integrated ECA on the inner wall of the curved microchannel, which we refer to as CIECA, to enhance particle inertial focusing. To elucidate the underlying mechanism of particle focusing in this integrated microchannel, we conducted numerical and experimental comparisons between CIECA and two other microchannels: COECA (ECA integrated along the outer wall of the curved microchannel) and SECA (straight microchannel with ECA). We observed that the velocity of the Dean flow induced by the ECA surpassed that induced by the curved microchannel, highlighting the significant role of the ECA in particle focusing. As a result, the majority of particles efficiently focused in the microchannel with ECA, with the equilibrium position located near the side in the same direction as the expansion region. The particles could be tightly focused

to form a narrow line in CIECA and the focusing width in CIECA was reduced to one-second of that in SECA and one-third of that in COECA. This reduction resulted from the consistent direction of the Dean flow induced by these two structures in CIECA, where the coordinated alignment of Dean flow from both the ECA structure and the curved microchannel contributed to the efficient particle focusing. Furthermore, we explored the effect of the Reynolds number and particle diameter on particle focusing in these three microchannels. As the Reynolds number increased, the focusing performance gradually improved in CIECA and SECA, but deteriorated in COECA. Moreover, the focusing performance of CIECA surpassed that of SECA. For the influence of the particle diameter on focusing performance, CIECA exhibited the best-focusing performance among the three microchannels. In CIECA, as the particle size increases, the focusing width initially decreases and then increases. Among them, particles with diameters of 8 and 10  $\mu\text{m}$  can achieve complete focusing.

## 2 Methods

### 2.1 Experiment section

To maintain consistency in the Dean flows induced by both the ECA and the curved microchannel, the ECA is designed on the inner wall of the curved microchannel, as illustrated in Fig. 1a. The microchannel incorporates a total of 20 expansion–contraction arrays, with an overall length of 4.34 cm. The dimensions of COECA and SECA are identical to those of CIECA. These microchannels were fabricated using established soft-lithography techniques. Polydimethylsiloxane (PDMS) was selected as the material for microchannel fabrication and permanently bonded to a glass substrate through oxygen plasma treatment. The microchannel was formed by pouring a mixture of PDMS and its curing agent (in a 10:1 ratio) onto molds and then curing it for 1 h at a constant temperature of 80  $^{\circ}\text{C}$  in a convection oven. The molds for the microchannel were produced on a silicon substrate by exposing the photoresist SU-8.

The particles used in this study were 10  $\mu\text{m}$  polystyrene particles. To prevent undesirable particle sedimentation, a mixture of glycerol and deionized water was prepared at a volume ratio of 2.2:7.8 (Kim and Yoo 2008). Moreover, Tween 20 was added to the glycerol–water mixture at a concentration of 0.01% w/v to inhibit particle aggregation and adhesion to the channel walls (Gou et al. 2020). Finally, the particle suspension was diluted to a concentration of 0.1% (w/v) using this mixture.

The experimental setup is illustrated in Fig. 2. The prepared particle suspension underwent a 10-min sonication process to achieve a suitably monodisperse suspension.

Subsequently, the suspension was introduced into the microchannel using a syringe pump (Lead Fluid, TYD01, China) at predetermined flow rates. For observing and tracking the particle trajectories, a high-speed camera (Fastec Image, His-pec5, German) was positioned beneath an inverted microscope (Optex Co. Ltd., BDS400, China), with the microfluidic device placed on the microscope stage. The high-speed camera meticulously captured the particle trajectories at precise intervals of 50 ms, ensuring accurate data recording on a computer for subsequent analysis and evaluation.

### 2.2 Numerical methods

To investigate the factors influencing particle focusing in these microchannels, we conducted computational fluid dynamics simulations to model the solid–liquid two-phase flow using the COMSOL Multiphysics software. These simulations enabled us to explore the diverse parameters that affect particle dynamics. Initially, we solved the continuity and Navier–Stokes equations for a single-phase incompressible flow, excluding particles, to obtain a steady flow field. The governing equations were formulated as follows:

$$\rho \nabla \cdot \mathbf{u} = 0, \quad (1)$$

$$\rho(\mathbf{u} \cdot \nabla)\mathbf{u} = \nabla \cdot [-p\mathbf{I} + \mu(\nabla\mathbf{u} + (\nabla\mathbf{u})^T)], \quad (2)$$

where  $\mathbf{u}$  represents the velocity vector,  $p$  denotes the pressure,  $\rho$  is the density and  $\mu$  represents the dynamic viscosity. The glycerol–water mixture has a density of approximately 1050  $\text{kg}\cdot\text{m}^{-3}$  and a viscosity range from 0.00145 to 0.00155 Pa s (Kim and Yoo 2008).

To precisely capture flow details, including the Dean flow, both the velocity and pressure fields were discretized using piecewise quadratic interpolation (Shiriny and Bayareh 2021) for solving the Navier–Stokes equations. At the inlet, a prescribed volume flow rate was specified, while an ambient pressure boundary condition was enforced at the outlet. Additionally, a no-slip boundary condition was imposed on the walls of the microchannel. These boundary conditions were implemented to ensure a realistic simulation of the fluid flow within the microchannel, facilitating the analysis of particle dynamics.

Utilizing the obtained flow field, Newton's second law was applied to predict the particle trajectories. This approach provided valuable insights into the migration process and spatial distribution of particles in the microchannel, thereby contributing to a comprehensive understanding of particle dynamics in the presence of the ECA.

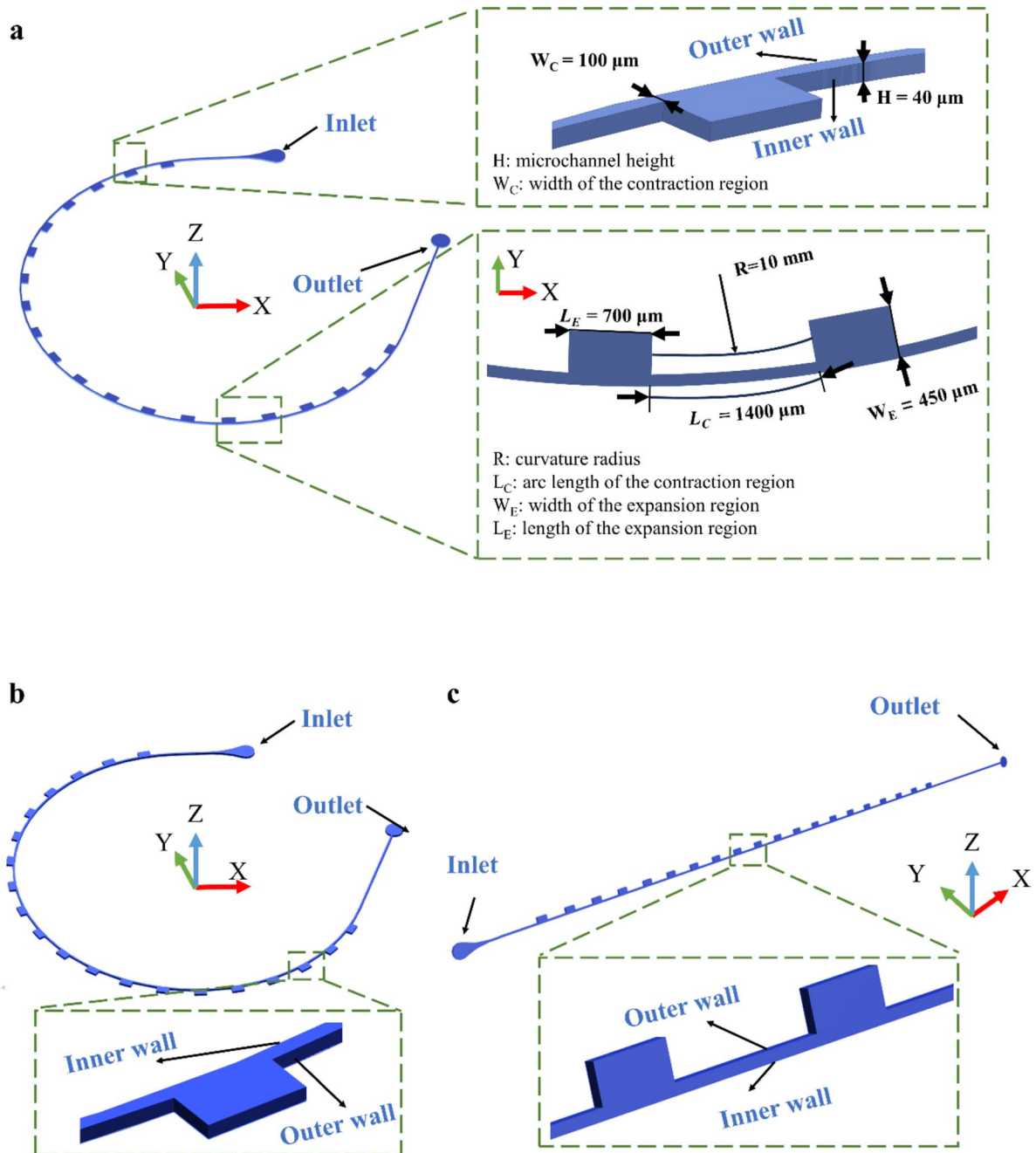


Fig. 1 a Schematic representation of the CIECA device structure and dimensions, along with schematic diagrams of b COECA and c SECA

$$m_p \frac{dV_p}{dt} = \frac{\pi \mu d_p C_D Re_s}{8} (\mathbf{u} - \mathbf{V}_p) + F_L + F_G, \quad (3)$$

where  $m_p$  and  $V_p$  are the mass and velocity of the particle, respectively, and the first term on the right side of the equation represents the drag force, where  $C_D$  is the drag coefficient which can be calculated by  $C_D = a_1 + \frac{a_2}{Re_s} + \frac{a_3}{Re_s^2}$

(Morsi and Alexander 1972).  $Re_s$  is the relative Reynolds number calculated by  $Re_s = \frac{\rho |u - V_p| d_p}{\mu}$ .  $F_G$  is neglected because the density of the particle is close to that of the sample fluid (Wang et al. 2024). The interaction force between particles was ignored to reduce the amount of computation due to the decreased particle concentration.  $F_L$

**Fig. 2** a Schematic of the particle focusing setup, along with images depicting the particle trajectory at the b inlet and c outlet

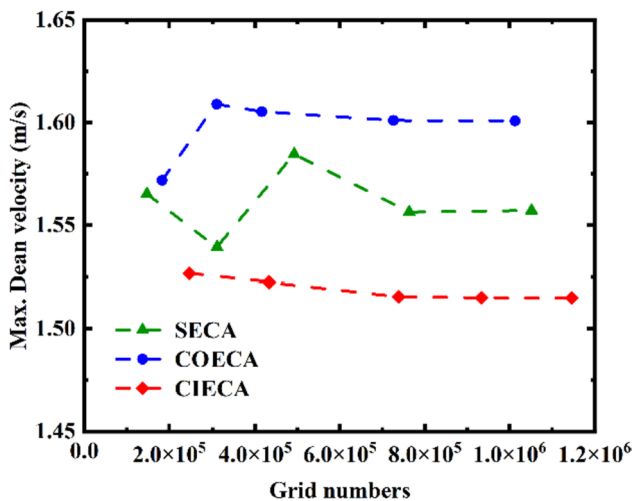
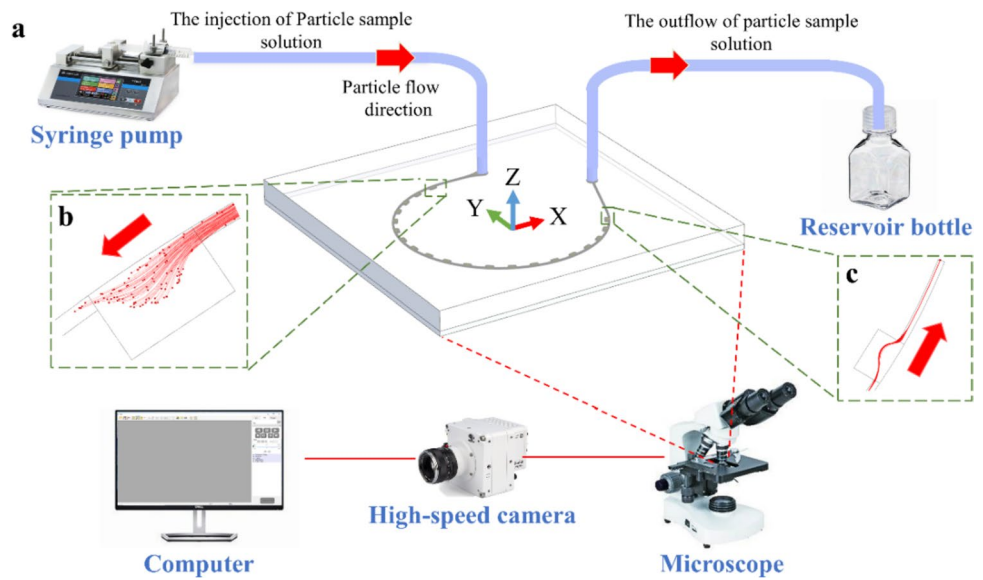


**Fig. 3** Maximum Dean velocity of the different microchannels at  $Re = 83.33$  for various grid numbers

is inertial lift force, which is calculated using the following equation:

$$F_L = (C_1 \beta^2 G_1 + C_2 \beta \gamma G_2) \frac{\rho U_{max} r_p^4}{H^2}, \tag{4}$$

where  $\beta$  and  $\gamma$  are the dimensionless shear rate and the dimensionless shear gradient, respectively.  $G_1$  and  $G_2$  are the functions of the lateral position. The correction coefficients  $C_1$  and  $C_2$ , derived from direct numerical simulations, are suitable for a wide range of Reynolds numbers and aspect ratios ( $AR = W/H$ ) of the channel (Nasiri et al. 2020).

To ensure grid independence, we examined various grid numbers with tetrahedral mesh elements. The maximum Dean velocity generated by the ECA was computed for

three microchannels at a Reynolds number of 83.33. Figure 3 illustrates the relationship between the maximum Dean velocity and the number of grid elements. As the number of grid elements surpassed 700,000, the maximum Dean velocity values reached a plateau. Consequently, simulations were conducted using over 700,000 elements. The selection of grid configurations was based on their capability to accurately capture the flow dynamics within each microchannel.

### 2.3 Result measurement

To quantitatively assess the equilibrium position, we accurately calculated the average lateral equilibrium position of the particles using Eq. (5) (Lee et al. 2011). Experimental data were acquired from a stack of captured images ( $\geq 1000$  images) (Liu et al. 2016), depicting the distribution of microparticles. The substantial number of images ensured a robust particle population for comprehensive analysis.

$$\bar{Y} = \frac{\sum_{i=1}^n y_i I_i}{\sum_{i=1}^n I_i}, \tag{5}$$

where  $y_i$  represents the dimensionless lateral equilibrium position of each particle,  $\bar{Y}$  denotes the particle average lateral equilibrium position, and  $I_i$  signifies the grayscale values for the experiment or the particle number for simulation of each lateral position.

For a quantitative assessment of the width of particle focusing, we meticulously analyzed the dispersion of particle-focusing positions using the standard deviation of the lateral equilibrium position. The standard deviation, serving as a measure of the degree of particle dispersion, can be computed using the following equation:

$$\sigma = \sqrt{\frac{\sum_{i=1}^n I_i (y_i - \bar{Y})^2}{\sum_{i=1}^n I_i}} \quad (6)$$

Through the calculation of the standard deviation, we comprehensively assessed the width of particle focusing, offering valuable insights into the effectiveness and precision of the microchannel in achieving particle confinement and alignment.

To make the results more universal, we use the Reynolds number of the fluid in the contraction region to characterize the flow state of the fluid. In this paper, the range of Reynolds number is from 16.67 to 83.33. Correspondingly, the volume flow rate is from 100 to 500  $\mu\text{L}\cdot\text{min}^{-1}$ .

### 3 Result and discussion

#### 3.1 Flow field analysis

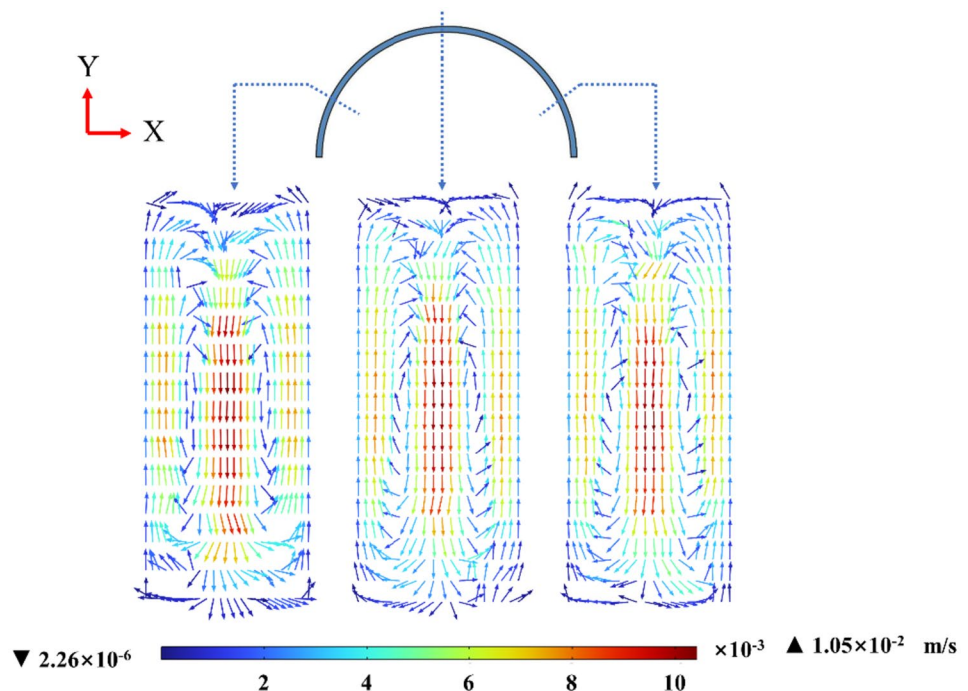
The particles in the microchannel experience inertial lift forces, comprising the shear gradient lift force and the wall-induced lift force. The shear gradient lift force propels particles toward the microchannel wall, while the wall-induced lift force drives these particles away from the microchannel wall (Di Carlo 2009). In addition to inertial lift forces, particles also undergo Dean drag forces in the curved microchannel or ECA. This Dean flow induces a lateral drag force on the particles, influencing their migration. Typically, for small particle sizes, the Dean flow drag force can be

greater than the lift force in the curved microchannel and ECA. In this section, we analyzed the Dean flow in the curved microchannel and ECA. The width of the curved microchannel is identical to the width of the contraction region in ECA. The fluid, including 10  $\mu\text{m}$  polystyrene particles, was injected into these microchannels using a syringe pump at flow rates of 500  $\mu\text{L}\cdot\text{min}^{-1}$  ( $\text{Re} = 83.33$ ).

In the curved microchannel, the fluid experiences a centrifugal effect, resulting in the generation of Dean flow in the cross section. Figure 4 depicts the velocity contours in different cross sections of the curved microchannel. As depicted, the maximum Dean flow velocity in each cross section is consistent, at approximately  $1.05 \times 10^{-2} \text{ m s}^{-1}$ . The Dean flow in the curved microchannel is relatively weak. As a result, traditional curved microchannels often necessitate lengthy designs or the assistance of sheath flows to enhance particle migration strength (Lee et al. 2011; Zhao et al. 2020).

To overcome this limitation, the ECA is employed to amplify the Dean flow in the cross section. To illustrate the dynamics of the cross-sectional flows within the straight ECA microchannel, we compared five extracted images depicting the flows in the cross section at different positions in the contraction region of ECA (Fig. 5). As observed, the microchannel's hydraulic diameter abruptly decreases, resulting in a significant velocity component in the cross section and the generation of the Dean flow when the fluid flows from the expansion region to the contraction region. The strength of the Dean flow is relatively high, reaching up to  $1.56 \text{ m s}^{-1}$ . The Dean flow gradually weakens as the fluid

**Fig. 4** Velocity fields of the Dean flow obtained by simulation at  $\text{Re} = 83.33$



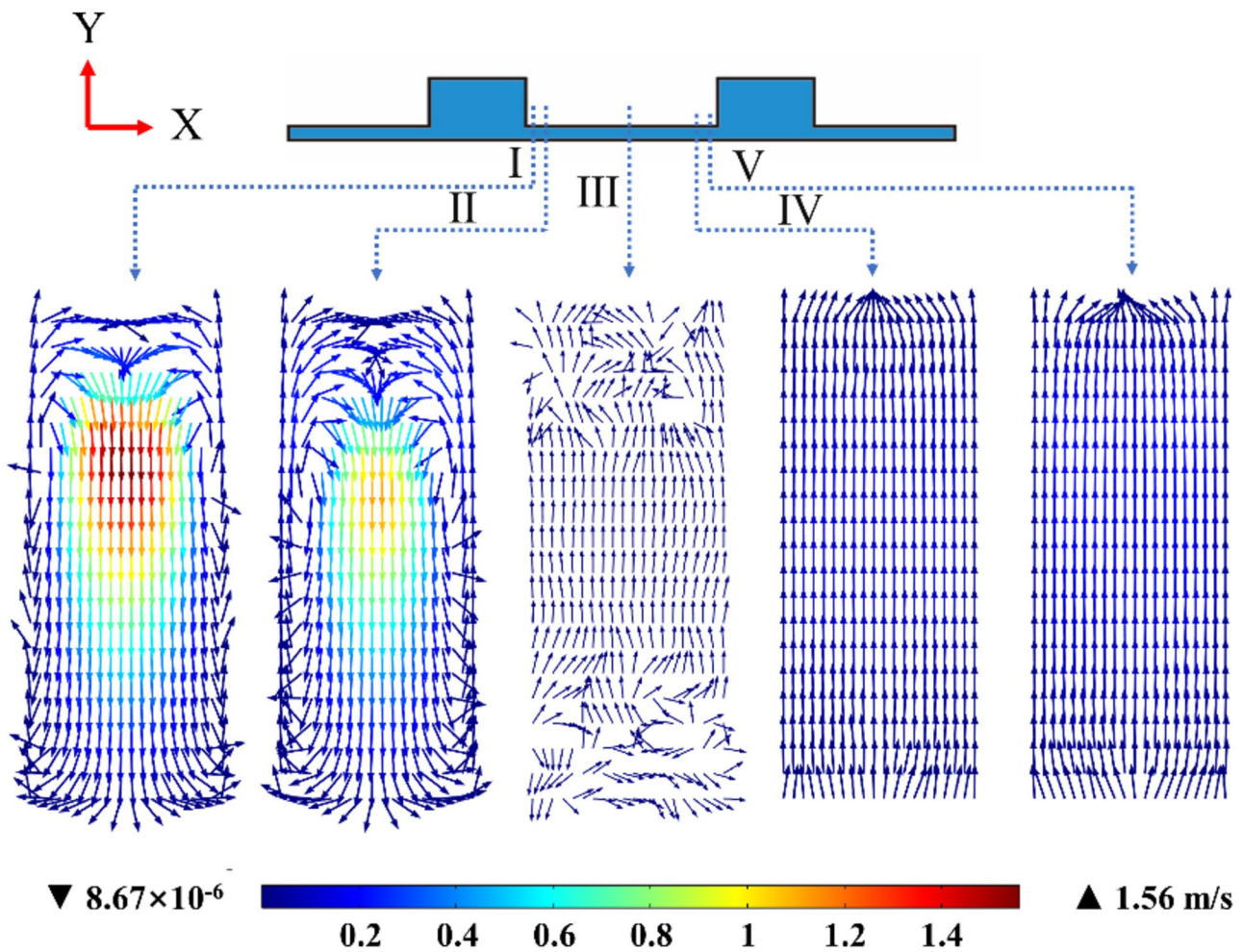


**Fig. 5** Velocity fields obtained by simulation at different cross-sections distanced from the beginning of the second contraction region with  $0.01L_C$  (I),  $0.02L_C$  (II),  $0.5L_C$  (III),  $0.98L_C$  (IV), and  $0.99L_C$  (V)

flows further into the contraction region, and its strength approaches zero after the fluid passes through the middle line of the contraction region. Conversely, as the fluid enters the expansion region, the velocity decelerates abruptly, effectively offsetting the Dean flow effects. Compared with the Dean flow in contraction, the Dean flow in the expansion region is relatively weak. Therefore, the Dean flow plays a crucial role in the contraction region of ECA for particle focusing.

The arrangement of these two geometries plays a crucial role in determining the direction of the secondary flow. As seen in Figs. 4 and 5, within the ECA structure, the transverse median fluid tends to flow toward the sides, opposing the direction of the expansion region. Additionally, due to the centrifugal effects, the curved channel generates a secondary flow in which the median fluid within the cross-sectional flows from the inner wall toward the outer wall. Consistency in the direction of

the secondary flow is essential for optimizing particle focusing. When the ECA structure is combined with the outer wall of the curved microchannel, the direction of the secondary flow is not consistent. The Dean flow of the curved microchannel weakens the migration effect produced by the ECA structure, resulting in poorer focusing performance. Therefore, ensuring consistency in the direction of the secondary flow induced by the two structures is crucial. We hypothesize that this combined structure can enhance the secondary flow and result in more rapid particle migration. Based on this hypothesis, we conducted both experimental and numerical investigations to study the inertial focusing of particles in CIECA.

Figure 6 illustrates the lateral dimensionless equilibrium position ( $\bar{Y}/W$ ) and dimensionless focusing width ( $\sigma/W$ ) at various Reynolds numbers. It can be seen that

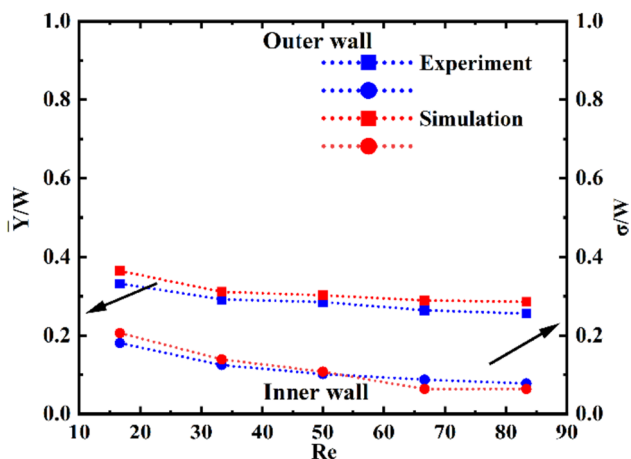


Fig. 6 Dimensionless equilibrium position and dimensionless focusing width of particles for different Reynolds numbers in the CIECA

the results of the experiment and numerical simulation were in good agreement, demonstrating the excellent accuracy of the proposed model. It also can be found that the particles can be focused well, although the total length of the integrated microchannel is only 4.34 cm. The dimensionless focusing width is as low as 0.170 when the Reynolds number is 16.67. As the Reynolds number increases, the focusing width becomes smaller, reaching 0.078 at a Reynolds number of 83.33. This means that the CIECA microchannel has exceptional particle-focusing performance.

### 3.2 Mechanism of particle focusing

To investigate the exceptional particle-focusing performance of the CIECA microchannel, we compared particle behavior in three different microchannels: CIECA, COECA, and SECA. All these microchannels were fabricated with equal dimensions. 10 μm polystyrene particles were selected to emulate white blood cells (Abdulla et al. 2018) and injected into these microchannels at flow rates of 500 μL·min<sup>-1</sup> (Re = 83.33).

As shown in Fig. 7a, it was observed that most particles could reach the equilibrium position in these three microchannels, but in the CIECA, the particles tightly focused to form a narrow line. The average dimensionless focusing width was 0.078 in the CIECA, smaller than 0.146 in the SECA. This indicated that the particles had a focusing width of 15.6 μm (2σ) within a channel with a width of 100 μm in the CIECA microchannel. Although the maximum Dean flow strength of the ECA structure was two orders of magnitude stronger than that of the curved microchannel, the focusing width of SECA was twice that of CIECA. This was because the Dean flow of the curved microchannel existed in each cross section, whereas it only existed in some cross sections in SECA. Moreover, the focusing performance in the traditional integrated microchannel of COECA was the worst, with focusing width about three times that in CIECA. This highlighted the crucial role of the integrated approach of Dean flow induced by the curved microchannel and ECA in particle focusing.

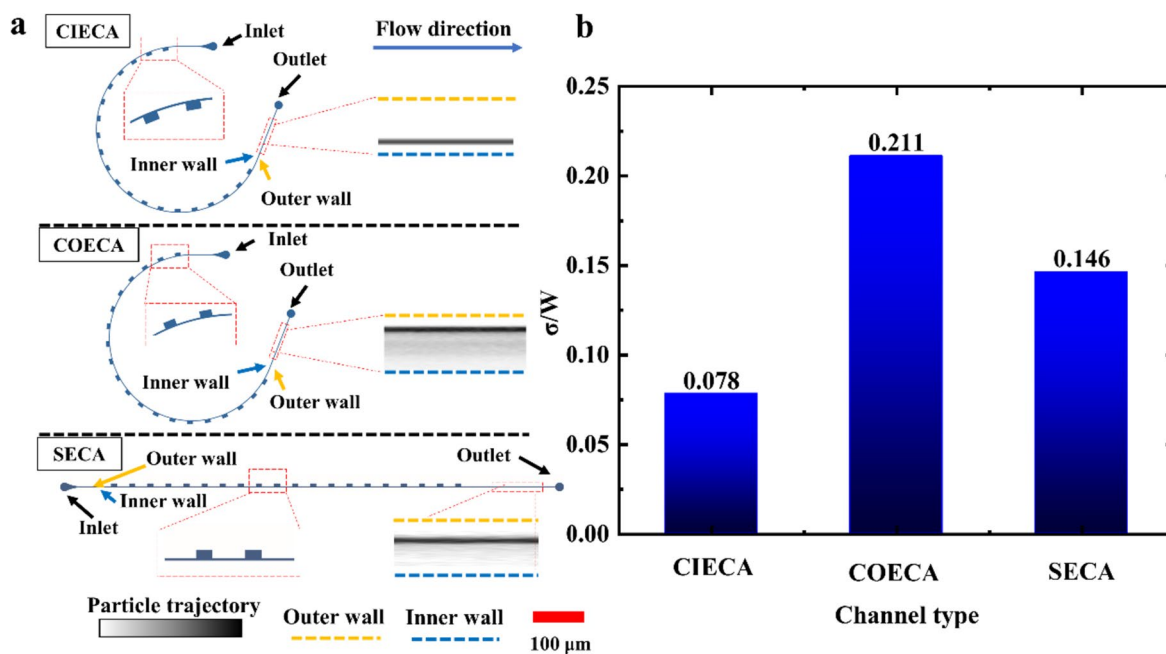


Fig. 7 a Visualization results of particle trajectories and b corresponding dimensionless focusing width of particles (experimental result)



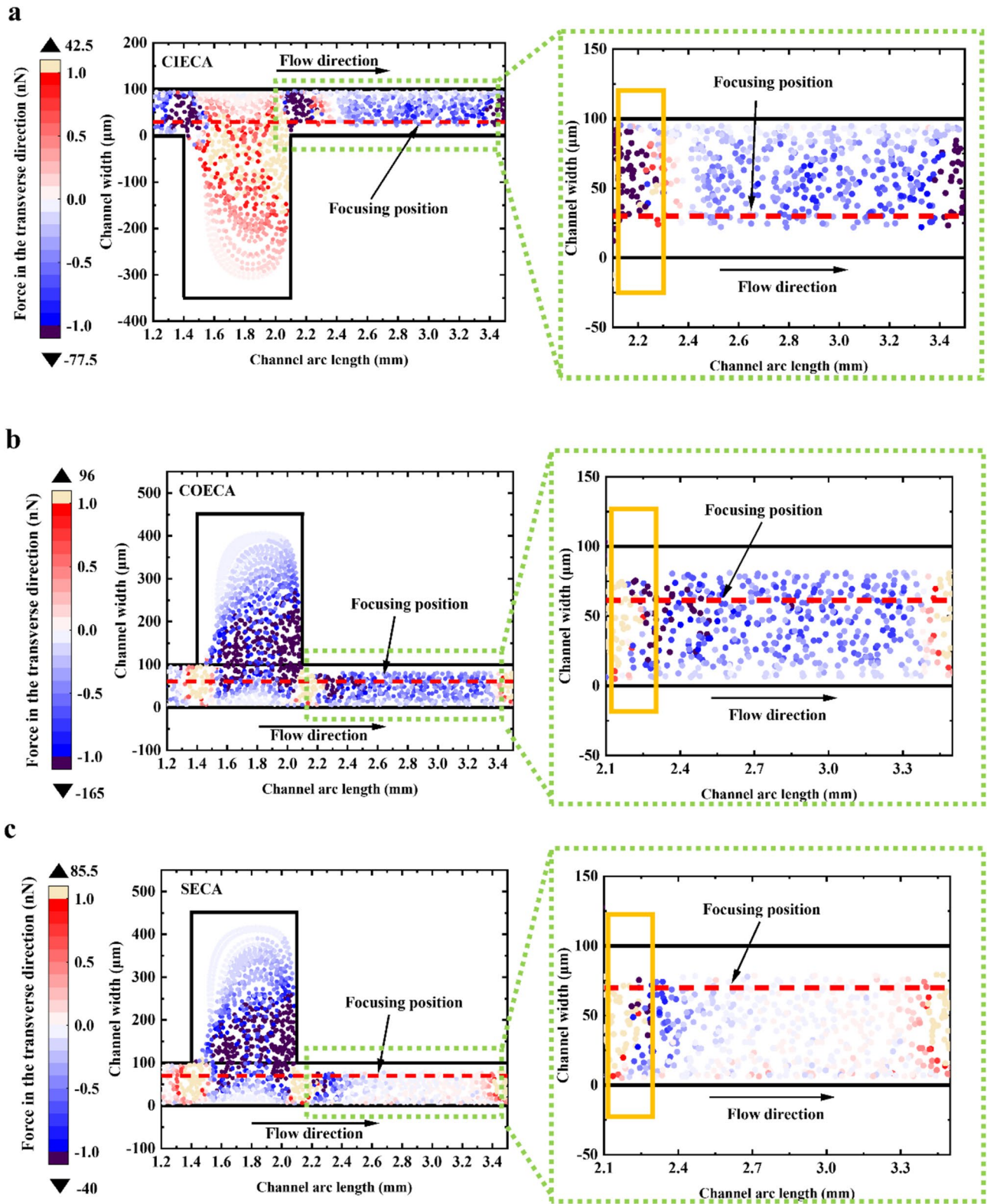


Fig. 8 Forces in the transverse direction acting on particles in the second EC region of **a** CIECA, **b** COECA, and **c** SECA (numerical result)

To gain a deeper understanding of the particle-focusing mechanism within these microchannels, numerical simulations were utilized to explore the fluid flow and particle dynamic. Figure 8 describes the forces in the  $y$ -direction acting on particles in the second EC region of each channel. The direction from the inner wall toward the outer wall was considered the positive direction of force. Conversely, it was regarded as the negative direction. From Fig. 8, in CIECA, from the end of the contraction region to the beginning of the expansion region, the channel width suddenly increased, leading to a rapid increase in fluid transverse velocity. Under the influence of drag force, particles also accelerated in the direction of expansion along with the fluid. Later, as the fluid velocity decreased, it dragged the particles to undergo decelerated curved motion. Due to the sudden decrease in width at the exit of the expansion region, the fluid rapidly contracted, inducing accelerated particle migration toward the contraction direction. The migration of particles within the expansion region did not contribute significantly to particle focusing. Therefore, the main particle focus was on the contraction region. According to Fig. 8, it can be observed that in all three channels, the forces at the entrance of the contraction region were much greater than in other parts of the contraction region. In SECA, the design resulted in smaller lateral forces in the contraction region, except at the entrance, compared to the other two microchannels. Consequently, we inferred that the focusing performance of CIECA was better than that of SECA, because the curved channel enhances the Dean flow in the contraction region, allowing particles to migrate to the focusing position more rapidly. In addition, in CIECA, the lateral forces on particles were all directed toward the focusing position (Fig. 8a). In COECA, the lateral force only points toward the focusing position at the entrance of the contraction region, while in other parts of the contraction region, it was in the opposite direction (Fig. 8b). Therefore, we believed that the exceptional particle-focusing performance of the CIECA microchannel was attributed to the synergy of the multi-Dean flow. The focusing performance was optimal for CIECA and poorest for COECA in these three microchannels.

To further support this speculation, the flow fields in three microchannels were analyzed and are shown in Fig. 9. In Fig. 9a, c, it was observed that in the middle of the contraction region of the straight microchannel, there was a second flow directed toward the outer wall in SECA and CIECA. The strength of this second flow in the contraction region of the straight microchannel was significantly lower (two orders of magnitude lower) than that of the Dean flow induced by the curved microchannel. As a result, some remote particles were not further accelerated toward the equilibrium position in the straight microchannel, but most particles could still focus, and the equilibrium position was near the side.

To confirm that the Dean flow induced by the curved microchannel and that generated by the ECA are consistent, we placed the ECA on the outer wall of the curved microchannel to ensure different Dean flow directions for these two structures. The experimental result showed that the dimensionless focus width was 0.211 (Fig. 8b), which was much poorer than that of CIECA. From the velocity contour (Fig. 9b), it could be observed that the Dean flow induced by the ECA and that induced by the curved microchannel were not consistent, and the maximum Dean flow which was induced by the ECA structure was two orders of magnitude greater than that induced by the curved microchannel. Therefore, most particles were able to achieve effective focusing, but the Dean flow generated by the curved microchannel strongly pushed some remote particles to migrate in the opposite direction of the equilibrium position, making it difficult for some particles located farther away to reach the focusing position.

### 3.3 Effect of Reynolds number on focusing performance

To further investigate the focusing performance, the influence of the Reynolds number on the focusing performance was analyzed in this section. Particles were injected into these microchannels at flow rates ranging from 100 to 500  $\mu\text{L}\cdot\text{min}^{-1}$ , corresponding to Reynolds numbers ranging from 16.67 to 83.33. At a Reynolds number of 83.33, the flow velocity in the contraction region reaches a maximum of 4.13  $\text{m}\cdot\text{s}^{-1}$ , which is exceptionally high for a microchannel. Therefore, we did not investigate scenarios with Reynolds numbers exceeding 83.33.

As depicted in Fig. 10, most particles in these microchannels focus on the equilibrium position at various Reynolds numbers. As the Reynolds number increased, the focusing positions moved closer to the wall where the expansion region was located. At  $\text{Re}=83.33$ , the particles in the CIECA were tightly focused to form a narrow line, whereas, in SECA and COECA, a few particles showed tendencies to defocus. As shown in Fig. 11, when Reynolds numbers increased from 16.67 to 83.33, the dimensionless focusing widths of the CIECA and SECA decreased from 0.170 to 0.078 and from 0.179 to 0.145, respectively, while the dimensionless focusing widths of the COECA increased from 0.169 to 0.211. This implied that within the 100  $\mu\text{m}$  width microchannel, the particle's focusing width in CIECA decreased from 34 to 15.6  $\mu\text{m}$ . In SECA, it decreased from 35.8 to 29.2  $\mu\text{m}$ , and the focusing width increased from 33.8 to 42.2  $\mu\text{m}$  in COECA.

To comprehend the influence of the Reynolds number on particle-focusing performance in the three channels, an analysis was performed using particles that were most challenging to attain the equilibrium position as representatives. This

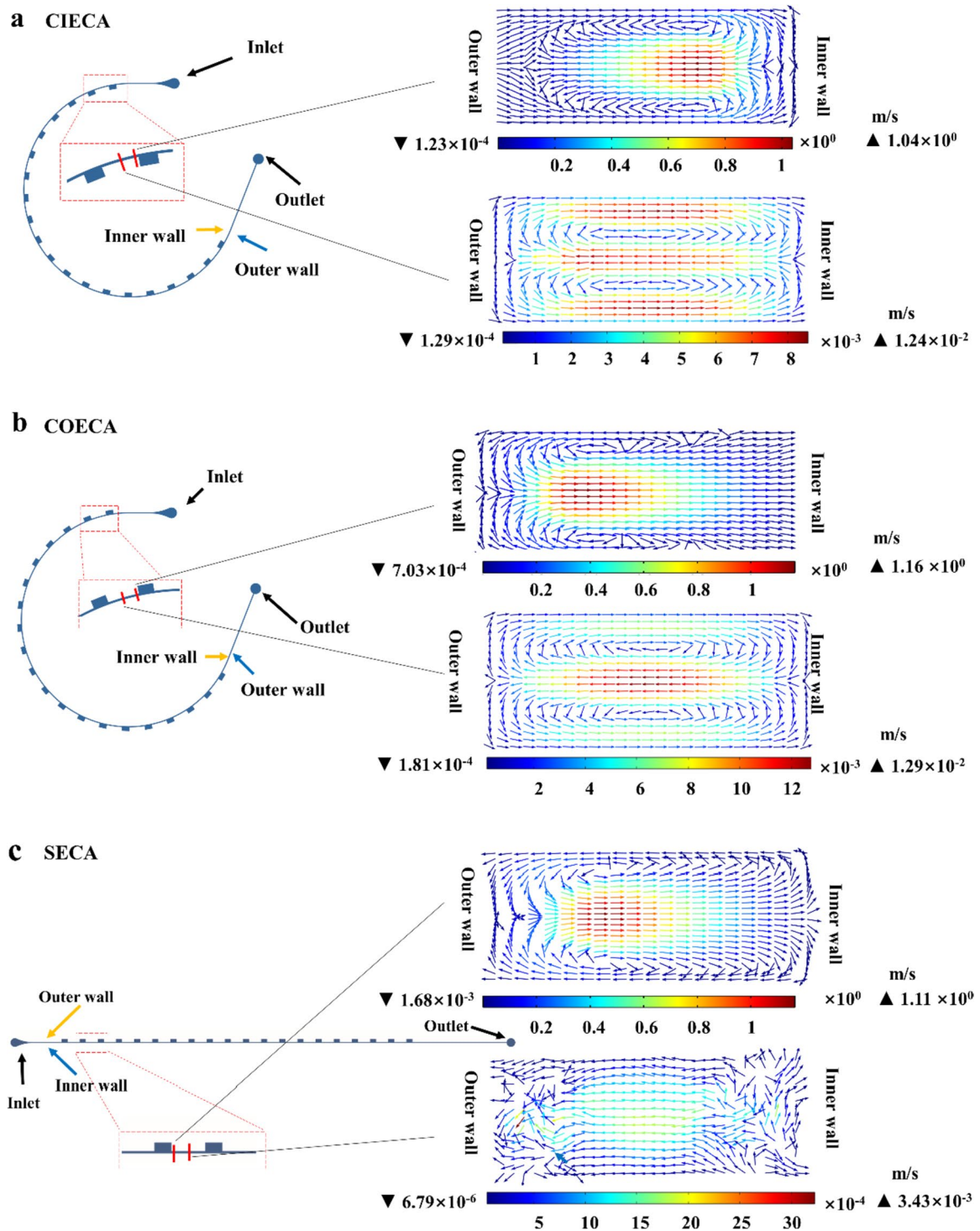


**Fig. 9** Transverse velocity fields of **a** CIECA, **b** COECA, and **c** SECA at  $Re = 83.33$  (numerical result)

was because the farthest particles necessitate a sufficiently large lateral force to swiftly migrate to the equilibrium position within the limited length of the channel. The lateral forces acting on particles located farthest from the equilibrium position (e.g., in CIECA, particles at a distance of

$5.9 \mu\text{m}$  from the outer wall) were integrated over the entire channel, and the average value was obtained, as shown in Fig. 12. The average lateral force on the particles in all three channels increased with the Reynolds number. As a result, the focusing positions of particles also moved closer to the

**Fig. 10** Experimental results of particle trajectories in **a** CIECA, **b** COECA, **c** and SECA at different Reynolds numbers

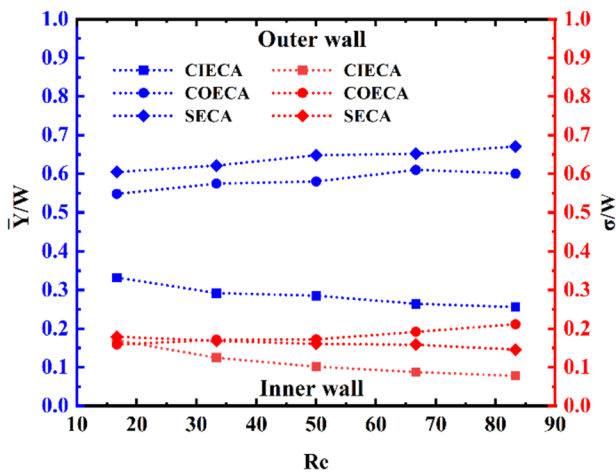
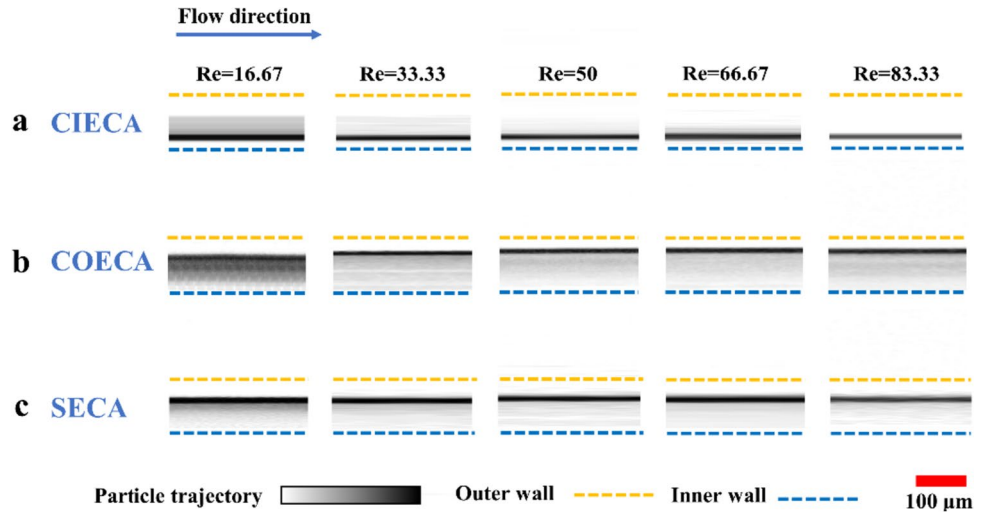


**Fig. 11** Experimental results of focusing positions and width at varying Reynolds numbers

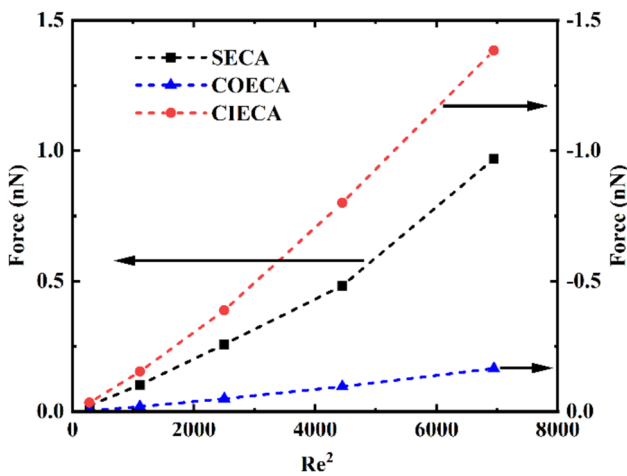


**Fig. 12** Average lateral force experienced by particles farthest from the equilibrium position at various Reynolds number in different channels (numerical results)

wall where the expansion region was located. From Fig. 12, it can be observed that the average lateral force on CIECA increased more rapidly with the Reynolds number, with an amplification factor proportional to the square of the Reynolds number. The square of the Reynolds number ranges from a minimum of 277.889 to a maximum of 6943.889, with an increase of approximately 25 times. Meanwhile, the lateral force on the particles increased from  $-0.034$  to  $-1.384$  nN, which was an increase of about 40 times. Therefore, according to  $y = \frac{1}{2}at^2$  and  $v = \frac{x_{arc}}{t}$ , it can be concluded that in a certain length of microchannel, as the flow velocity increased, particles experienced greater lateral forces, allowing them to reach the focusing position more quickly. In SECA, the minimum average lateral force was 0.023 nN, and the maximum was 0.969 nN, resulting in an increase of about 42 times. Therefore, with the increase in Reynolds number, particles in SECA could achieve better focusing. The lateral force on particles in the transverse direction in SECA was smaller than the average lateral force in CIECA. Hence, the focusing effect of CIECA was better than that of SECA. In COECA, the lateral force on particles increased from  $-0.005$  to  $-0.166$  nN, with an increase of approximately 37 times. However, the average lateral force on particles in COECA was the smallest in these three microchannel and the direction of the force on particles did not point toward the focusing position. This leads to a deteriorating particle-focusing performance in COECA as the Reynolds number increases. As the fluid remains in a laminar flow state, particles in COECA continued to exhibit poor focusing performance even with an increase in Reynolds number.

### 3.4 Effect of the particle diameter on the focusing performance

To characterize the effect of particle diameter on the focusing performance, numerical simulations were conducted

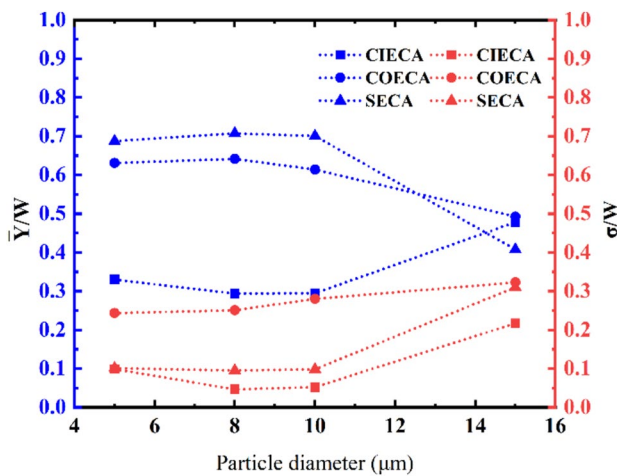


**Fig. 13** Numerical results of focusing positions and focusing widths for 5, 8, 10, and 15 μm particles

to calculate the flow trajectories of particles with different diameters in these three channels. As red blood cells typically range in size from 6 to 8 μm and white blood cells fall within the range of 10–12 μm (Shiriny and Bayareh 2021), 5, 8, 10, and 15 μm particles were injected into these three microchannels at flow rates of 500 μL·min<sup>-1</sup> (Re = 83.33). In Fig. 13, among these three channels, the focusing performance of 5–15 μm particles was the best in CIECA and the poorest in COECA. The focusing performance of particles in SECA was approximately similar to that in CIECA, but the focusing performance of CIECA was superior to that of SECA. Simultaneously, dimensionless focusing positions and focusing widths were calculated for particles of different diameters in these three channels. In the CIECA and SECA channels, within the particle diameter range of 5–10 μm, larger particle diameters resulted in focusing positions closer to the channel walls and smaller focusing widths (Fig. 13). However, for 15 μm particles, they tended to be more biased toward the center of the channel. The dimensionless focusing width trends in SECA and COECA are similar, decreasing initially and then increasing. In CIECA, the dimensionless focusing widths for 5, 8, 10, and 15 μm particles were 0.099, 0.047, 0.052 and 0.217, respectively. The focusing width for 5 μm particles was 19.8 μm, which was four times the particle diameter indicating relatively poor focusing performance. The focusing width for 15 μm particles was 43.4 μm, which was around 2.9 times the particle diameter, and the focusing widths for 8 and 10 μm particles within a 100 μm width channel were 9.4 and 10.4 μm, respectively, achieving single-particle focusing.

The focusing width of 5 μm particles was relatively large. This was mainly attributed to the small particle size of 5 μm, resulting in a smaller lateral force in the transverse direction, as indicated by Eqs. (3) and (4). In

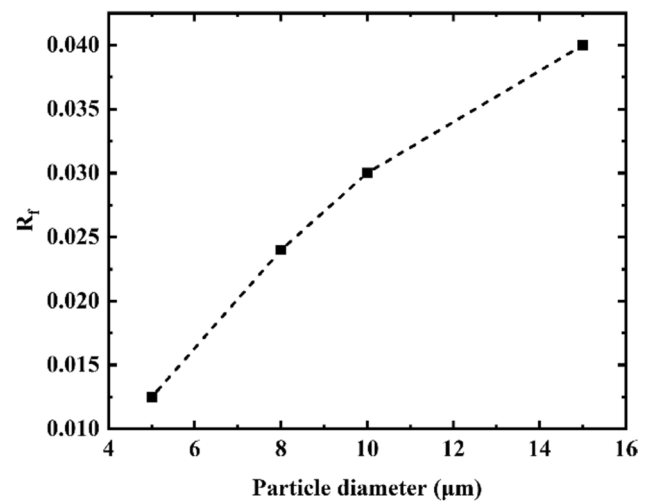


**Fig. 14** In CIECA,  $R_f$  values for particles with diameters of 5, 8, 10, and 15 μm (numerical result)

the same channel, this may hinder timely migration to the equilibrium position. Therefore, to enhance the focusing performance of 5 μm particles, one approach could be to extend the channel length. From Fig. 15a, it is observed that the focusing performance of 5 μm particles significantly improved with the elongation of the channel. The dimensionless focusing width reduced from 0.099 to 0.043, as shown in Fig. 15b. This implied that the focusing width decreased from 19.8 to 8.6 μm for 5 μm particles, enabling single-particle focusing. With the increase in particle size, the lateral forces acting on the particles gradually increased. Therefore, 8 and 10 μm particles more fully migrate to the equilibrium position under the synergistic Dean flow in CIECA. However, as the particle size increases, the larger  $R_f = \frac{F_L}{F_D}$  values indicate that the inertial lift force grows faster compared to the Dean drag force (Fig. 14). The effect of the Dean flow began to weaken, causing 15 μm particles to migrate to the equilibrium position more slowly. Due to the larger focusing width of 15 μm particles, their dimensionless focusing position was closer to the middle of the channel.

In SECA, the dimensionless focusing widths for 5, 8, 10, and 15 μm particles were 0.101, 0.095, 0.098 and 0.310, respectively. Compared to CIECA, the focusing performance of SECA was inferior. This was mainly because the secondary flow intensity was only significant at the entrance of the contraction region in SECA, while it was weaker in other parts, hindering further particle migration to reach the equilibrium position. The other contraction region could not further promote the migration of particles to reach the equilibrium position. Moreover,

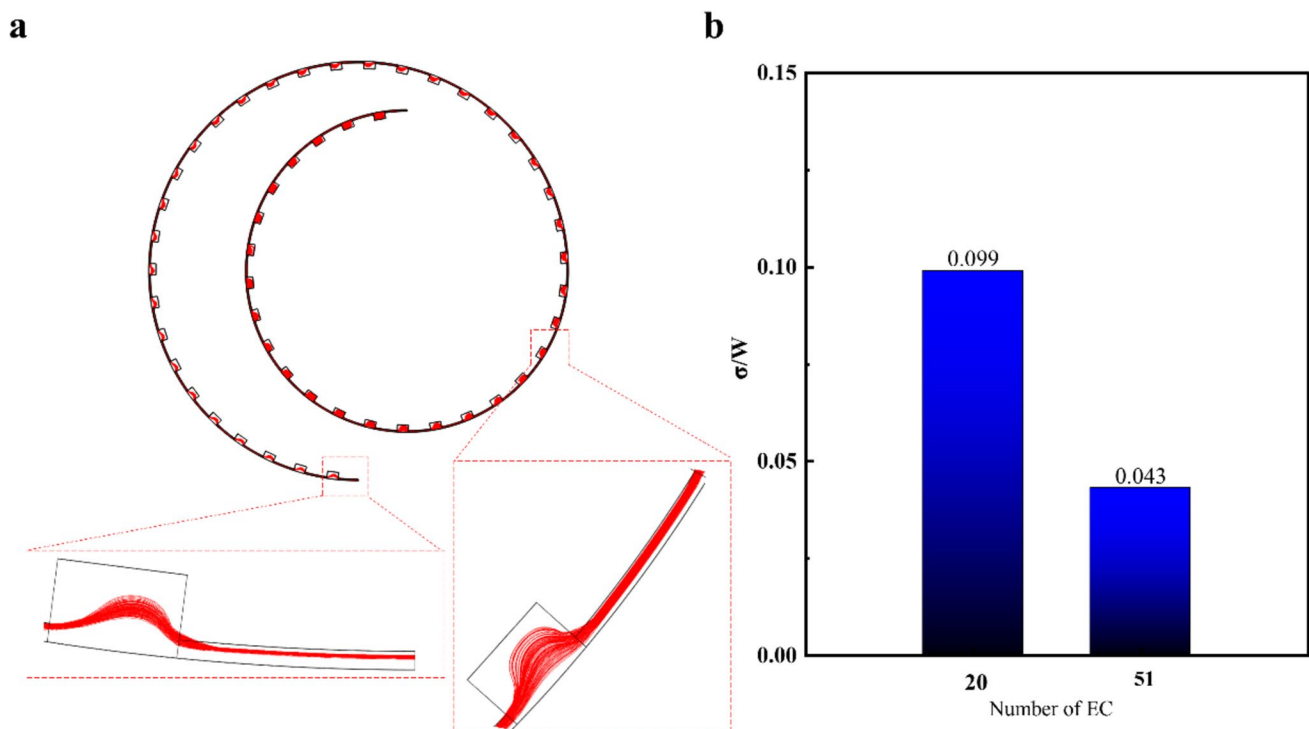


**Fig. 15** Numerical results of **a** migration trajectory and **b** focusing width of 5  $\mu\text{m}$  particles

the focusing position in CIECA was closer to the channel wall compared to SECA, attributed to the coordinated enhancement of the two Dean flows, promoting more effective particle migration. In COECA, the dimensionless focusing widths for 5, 8, 10, and 15  $\mu\text{m}$  particles were 0.243, 0.251, 0.280 and 0.322, respectively. The Dean flow induced by ECA and the Dean flow induced by the curved channel had inconsistent directions. As the particle size increased, the force acting on the particles in the transverse direction became stronger, leading to a larger particle-focusing width. As a result, the focusing performance of particles was poorer (Fig. 13).

## 4 Conclusion

In this study, we proposed the CIECA microchannel to enhance particle-focusing performance and studied its focusing mechanism through a combined approach of experiments and numerical simulations. The focusing performance of CIECA was the best among the three microchannels (CIECA, SECA, and COECA) due to the consistency of the Dean flow induced by the curved channel and ECA. The focusing performance for COECA was worst because the Dean flows induced by the ECA structure and curved microchannel were inconsistent. The focusing width in the proposed microchannel was about only about

1/3 of that in the traditional microchannel of COECA, and 1/2 of that in the SECA. Moreover, it was found that the dimensionless focusing width in CIECA and SECA decreased from 0.170 to 0.078 and from 0.179 to 0.146 as the Reynolds number increased, respectively. The improvement in focusing performance with the increase of the Reynolds number could be attributed to the fact that, as the Reynolds number increased, particles generate larger lateral forces, prompting them to reach the focusing position more quickly. Therefore, in CIECA and SECA, the particle-focusing performance improved as the Reynolds number increased. However, in SECA, the average lateral force on particles was smaller than that in CIECA. Therefore, SECA exhibited relatively poorer focusing performance with changes in Reynolds number compared to CIECA. In COECA, the average lateral force on particles in COECA was the smallest in these three microchannels and the average lateral force direction on particles did not point toward the focusing position. As a result, particles had difficulty migrating to the focusing position, leading to poorer focusing performance in this channel. Numerical simulations were conducted to calculate the trajectories of particles with different diameters in these three channels. Due to the synergistic effect of the Dean flow, CIECA exhibited better focusing performance for particles of various sizes compared to the other two channels, with COECA being the least effective. In CIECA, for 8 and 10  $\mu\text{m}$  particles, the dimensionless focusing widths

were 0.047 and 0.052, allowing for single-particle focusing. However, for 5 and 15  $\mu\text{m}$  particles, the dimensionless focusing widths were 0.099 and 0.217. Smaller particles experienced weaker lateral forces, while larger particles like 15  $\mu\text{m}$  were influenced more by inertial lift, leading to a decrease in the effect of Dean forces and slower particle migration, resulting in poorer focusing performance. The issue, particularly observed in the case of 5  $\mu\text{m}$  and 15  $\mu\text{m}$  particles, can be addressed by extending the channel length. This adjustment facilitated more effective particle migration and improved the focusing performance. This study served as a valuable reference for leveraging the synergistic effects of multi-Dean flow to enhance particle focusing. In comparison to traditional microchannels, the CIECA demonstrated efficient particle focusing within a shorter length of 4.34 cm, which is advantageous for applications requiring compact and effective particle manipulation.

**Acknowledgements** The authors acknowledge the financial support of the Key Laboratory of Low-grade Energy Utilization Technologies and Systems (No. LLEUTS-202312), the National Natural Science Foundation of China (Nos. 52106212, U20A20299, 51806038), the Natural Science Foundation of Guangdong Province (No. 2019A1515012119).

**Author contributions** RZ: methodology, formal analysis, investigation, writing—review and editing. KS: formal analysis, investigation, writing—review and editing. ZW: methodology, validation, formal analysis, investigation, writing—review and editing. GC: methodology, validation, formal analysis, writing—review and editing. YC: conceptualization, methodology, supervision. LJ: formal analysis, validation.

**Data availability** The data that support the findings of this study are available within the article and its supplementary material.

## Declarations

**Conflict of interest** The authors declare no competing interests.

## References

- Abdulla A, Liu W, Gholamipour-Shirazi A et al (2018) High-throughput isolation of circulating tumor cells using cascaded inertial focusing microfluidic channel. *Anal Chem* 90:4397–4405. <https://doi.org/10.1021/acs.analchem.7b04210>
- Augustsson P, Magnusson C, Nordin M et al (2012) Microfluidic, label-free enrichment of prostate cancer cells in blood based on acoustophoresis. *Anal Chem* 84:7954–7962. <https://doi.org/10.1021/ac301723s>
- Bhagat AAS, Kuntaegowdanahalli SS, Papautsky I (2008) Enhanced particle filtration in straight microchannels using shear-modulated inertial migration. *Phys Fluids* 20:101702. <https://doi.org/10.1063/1.2998844>
- Bhagat AAS, Kuntaegowdanahalli SS, Kaval N et al (2010) Inertial microfluidics for sheath-less high-throughput flow cytometry. *Biomed Microdevices* 12:187–195. <https://doi.org/10.1007/s10544-009-9374-9>
- Çetin B, Li D (2011) Dielectrophoresis in microfluidics technology. *Electrophoresis* 32:2410–2427. <https://doi.org/10.1002/elps.20110167>
- Di Carlo D (2009) Inertial microfluidics. *Lab Chip* 9:3038. <https://doi.org/10.1039/b912547g>
- Fan L-L, Wu X, Zhang H et al (2019) Continuous sheath-free focusing of microparticles in viscoelastic and Newtonian fluids. *Microfluid Nanofluidics* 23:117. <https://doi.org/10.1007/s10404-019-2281-3>
- Forbes TP, Forry SP (2012) Microfluidic magnetophoretic separations of immunomagnetically labeled rare mammalian cells. *Lab Chip* 12:1471. <https://doi.org/10.1039/c2lc40113d>
- Gou Y, Zhang S, Sun C et al (2020) Sheathless inertial focusing chip combining a spiral channel with periodic expansion structures for efficient and stable particle sorting. *Anal Chem* 92:1833–1841. <https://doi.org/10.1021/acs.analchem.9b03692>
- Guan G, Wu L, Bhagat AA et al (2013) Spiral microchannel with rectangular and trapezoidal cross-sections for size based particle separation. *Sci Rep* 3:1475. <https://doi.org/10.1038/srep01475>
- Jin C, McFaul SM, Duffy SP et al (2014) Technologies for label-free separation of circulating tumor cells: from historical foundations to recent developments. *Lab Chip* 14:32–44. <https://doi.org/10.1039/C3LC50625H>
- Kim YW, Yoo JY (2008) The lateral migration of neutrally-buoyant spheres transported through square microchannels. *J Micromech Microeng* 18:065015. <https://doi.org/10.1088/0960-1317/18/6/065015>
- Lee MG, Choi S, Park J-K (2009) Three-dimensional hydrodynamic focusing with a single sheath flow in a single-layer microfluidic device. *Lab Chip* 9:3155. <https://doi.org/10.1039/b910712f>
- Lee MG, Choi S, Park J-K (2011) Inertial separation in a contraction–expansion array microchannel. *J Chromatogr A* 1218:4138–4143. <https://doi.org/10.1016/j.chroma.2010.11.081>
- Li M, Muñoz HE, Schmidt A et al (2016) Inertial focusing of ellipsoidal *Euglena gracilis* cells in a stepped microchannel. *Lab Chip* 16:4458–4465. <https://doi.org/10.1039/C6LC01118G>
- Lim EJ, Ober TJ, Edd JF et al (2012) Visualization of microscale particle focusing in diluted and whole blood using particle trajectory analysis. *Lab Chip* 12:2199. <https://doi.org/10.1039/c2lc21100a>
- Liu C, Hu G, Jiang X, Sun J (2015) Inertial focusing of spherical particles in rectangular microchannels over a wide range of Reynolds numbers. *Lab Chip* 15:1168–1177. <https://doi.org/10.1039/C4LC01216J>
- Liu C, Xue C, Sun J, Hu G (2016) A generalized formula for inertial lift on a sphere in microchannels. *Lab Chip* 16:884–892. <https://doi.org/10.1039/C5LC01522G>
- Lu X, Liu C, Hu G, Xuan X (2017) Particle manipulations in non-Newtonian microfluidics: a review. *J Colloid Interface Sci* 500:182–201. <https://doi.org/10.1016/j.jcis.2017.04.019>
- Morsi SA, Alexander AJ (1972) An investigation of particle trajectories in two-phase flow systems. *J Fluid Mech* 55:193. <https://doi.org/10.1017/S0022112072001806>
- Nasiri R, Shamloo A, Akbari J et al (2020) Design and simulation of an integrated centrifugal microfluidic device for CTCs separation and cell lysis. *Micromachines* 11:699. <https://doi.org/10.3390/mi11070699>
- Prohm C, Stark H (2014) Feedback control of inertial microfluidics using axial control forces. *Lab Chip* 14:2115. <https://doi.org/10.1039/c4lc00145a>
- Qin J, Wang Z, Chen Y et al (2023) Thermocapillary flow-induced core release from double-emulsion droplets in microchannels. *Droplet* 2:54. <https://doi.org/10.1002/DRO2.54>
- Roper MG (2016) Cellular analysis using microfluidics. *Anal Chem* 88:381–394. <https://doi.org/10.1021/acs.analchem.5b04532>
- Segré G, Silberberg A (1961) Radial particle displacements in Poiseuille flow of suspensions. *Nature* 189:209–210. <https://doi.org/10.1038/189209a0>

- Shamloo A, Abdorahimzadeh S, Nasiri R (2019) Exploring contraction–expansion inertial microfluidic-based particle separation devices integrated with curved channels. *AIChE J* 65:16741. <https://doi.org/10.1002/aic.16741>
- Shen S, Tian C, Li T et al (2017) Spiral microchannel with ordered micro-obstacles for continuous and highly-efficient particle separation. *Lab Chip* 17:3578–3591. <https://doi.org/10.1039/C7LC00691H>
- Shen S, Zhang F, Wang S et al (2019) Ultra-low aspect ratio spiral microchannel with ordered micro-bars for flow-rate insensitive blood plasma extraction. *Sens Actuators B Chem* 287:320–328. <https://doi.org/10.1016/j.snb.2019.02.066>
- Shiriny A, Bayareh M (2021) Inertial focusing of CTCs in a novel spiral microchannel. *Chem Eng Sci* 229:116102. <https://doi.org/10.1016/j.ces.2020.116102>
- Tang W, Zhu S, Jiang D et al (2020) Channel innovations for inertial microfluidics. *Lab Chip* 20:3485–3502. <https://doi.org/10.1039/D0LC00714E>
- Wang Z, Li S, Chen R et al (2018) Numerical study on dynamic behaviors of the coalescence between the advancing liquid meniscus and multi-droplets in a microchannel using CLSVOF method. *Comput Fluid* 170:341–348. <https://doi.org/10.1016/j.compfluid.2018.05.014>
- Wang R, Sun S, Wang W, Zhu Z (2019) Investigation on the thermophoretic sorting for submicroparticles in a sorter with expansion–contraction microchannel. *Int J Heat Mass Transf* 133:912–919. <https://doi.org/10.1016/j.ijheatmasstransfer.2018.12.126>
- Wang Z, Zhen T, Wu F et al (2023) Enhanced particle focusing and sorting by multiple sheath stream in contraction–expansion microchannel. *Microfluid Nanofluidics* 27:16. <https://doi.org/10.1007/s10404-022-02620-5>
- Wang Z, Li Z, Jia L et al (2024) Numerical investigation on heat transfer characteristics of microencapsulated phase change material slurry in a rectangular minichannel. *J Therm Sci*. <https://doi.org/10.1007/s11630-024-1860-0>
- Xiang N, Wang J, Li Q et al (2019) Precise size-based cell separation via the coupling of inertial microfluidics and deterministic lateral displacement. *Anal Chem* 91:10328–10334. <https://doi.org/10.1021/acs.analchem.9b02863>
- Zhang J, Yan S, Yuan D et al (2016) Fundamentals and applications of inertial microfluidics: a review. *Lab Chip* 16:10–34. <https://doi.org/10.1039/C5LC01159K>
- Zhao Q, Yuan D, Zhang J, Li W (2020) A review of secondary flow in inertial microfluidics. *Micromachines* 11:461. <https://doi.org/10.3390/mi11050461>
- Zhou J, Papautsky I (2013) Fundamentals of inertial focusing in microchannels. *Lab Chip* 13:1121. <https://doi.org/10.1039/c2lc41248a>

**Publisher's Note** Springer Nature remains neutral with regard to jurisdictional claims in published maps and institutional affiliations.

Springer Nature or its licensor (e.g. a society or other partner) holds exclusive rights to this article under a publishing agreement with the author(s) or other rightsholder(s); author self-archiving of the accepted manuscript version of this article is solely governed by the terms of such publishing agreement and applicable law.